Available online at www.sciencedirect.com

ScienceDirect

www.elsevier.com/locate/jes

JES JOURNAL OF ENVIRONMENTAL SCIENCES

www.jesc.ac.cn

# Heterogeneous photocatalytic degradation of diuron on zinc oxide: Influence of surface-dependent adsorption on kinetics, degradation pathway, and toxicity of intermediates

*Sutaporn Meephon*[1], *Thanyada Rungrotmongkol*[2,3], *Somchintana Puttamat*[4], *Supareak Praserthdam*[5], *Varong Pavarajarn*[1,6,*]

1. *Center of Excellence in Particle Technology, Department of Chemical Engineering, Faculty of Engineering, Chulalongkorn University, Bangkok 10330, Thailand*
2. *Biocatalyst and Environmental Biotechnology Research Unit, Department of Biochemistry, Faculty of Science, Chulalongkorn University, Bangkok 10330, Thailand*
3. *Bioinformatics and Computational Biology Program, Graduated School, Chulalongkorn University, Bangkok 10330, Thailand*
4. *Department of Chemistry, Faculty of Science, Thammasat University, Pathumthani 12120, Thailand*
5. *Center of Excellence on Catalysis and Catalytic Reaction Engineering, Department of Chemical Engineering, Faculty of Engineering, Chulalongkorn University, Bangkok 10330, Thailand*
6. *Research Program in Hazardous Substance Management in Agricultural Industry, Center of Excellence on Hazardous Substance Management (HSM), Bangkok 10330, Thailand*

ARTICLE INFO

*Article history:*
Received 22 December 2018
Revised 4 April 2019
Accepted 15 April 2019
Available online 25 April 2019

*Keywords:*
Diuron
Photocatalysis
Adsorption
Degradation pathway
Mechanism
Toxicity

ABSTRACT

Heterogeneous photocatalytic reaction has been generally applied for degradation of toxic contaminants. Degradations of a compound using the same kind of catalyst that was synthesized differently are commonly found in literature. However, the reported degradation intermediates are normally inconsistent. This issue is especially important for the degradation of toxic compounds because intermediates may be more toxic than their parent compounds and understanding the reason is necessary if appropriate catalysts are to be designed. This work systematically compares the photocatalytic degradation of diuron, a toxic recalcitrant herbicide, on two forms of zinc oxide (ZnO), i.e., conventional particles with zinc- and oxygen-terminated polar surfaces as the dominating planes, and nanorods with mixed-terminated nonpolar surfaces. Experimental and theoretical results indicate that both the rate of reaction and the degradation pathway depend on the adsorption configuration of diuron onto the surface. Diuron molecules adsorb in different alignments on the two surfaces, contributing to the formation of different degradation intermediates. Both the aliphatic and aromatic sides of diuron adsorb on the polar surfaces simultaneously, leading to an attack by hydroxyl radicals from both ends. On the other hand, on the mixed-terminated surface, only the aliphatic part adsorbs and is degraded. The exposed surface is therefore the key factor controlling the degradation pathway. For diuron degradation on ZnO, a catalyst confined to

* *Corresponding author. E-mail:* Varong.P@chula.ac.th. (Varong Pavarajarn).

https://doi.org/10.1016/j.jes.2019.04.016

mixed-terminated surfaces, i.e., ZnO nanorods, is more desirable, as it avoids the formation of intermediates with potent phytotoxicity and cytogenotoxicity.


## Introduction

Toxic herbicides are widely used in agricultural regions. Leaching of residual herbicides into surface and underground water causes serious contamination and environmental problems. One of the most highly persistent and toxic herbicides is diuron (3-(3,4-dichlorophenyl)-1,1-dimethyl urea). It has a half-life of over 370 days in ecological environments (Bouquet-Somrani et al., 2000) and has caused serious contamination problems in many countries (King et al., 2013; Dabrowski et al., 2014; Hall and Anderson, 2014). Although conventional techniques, such as biodegradation and adsorption, have been applied in an attempt to remove diuron from water (Tixier et al., 2000; Sun et al., 2012), the acute toxicity of diuron toward living organisms including microorganisms (Hasenbein et al., 2017), and its typically low concentration in water, render these techniques ineffective.

Heterogeneous photocatalysis is an advanced oxidation process that is effective in removal of recalcitrant contaminants in water (Prieto-Rodriguez et al., 2012). The process relies on oxidation of the adsorbed pollutant by highly active hydroxyl radicals (OH•), which are produced when the catalyst is activated by light with photon energy higher than the catalyst's bandgap (Wang and Xu, 2012). Although the detailed mechanism of the generation of hydroxyl radicals is a matter of controversy (Montoya et al., 2014), it is generally accepted that, in aqueous solution, photogenerated holes ($h^+$) normally react with the abundant water molecules to form hydroxyl radicals (Lawless et al., 1991). Consequently, direct oxidation of the pollutant by the holes is negligible. The attack of hydroxyl radicals on an organic compound leads to its degradation, and eventually its total mineralization, but usually involves several intermediates. The photocatalytic degradation of diuron on $TiO_2$ has been investigated in several studies (Krysova et al., 1998; Malato et al., 2003; Carrier et al., 2009). Interestingly, these reports differ with respect to the nature of the intermediates. This discrepancy must be addressed if appropriate catalysts are to be designed. This is especially important for the degradation of toxic compounds such as diuron because some intermediates may be more toxic than their parent compounds (Evgenidou et al., 2006; Woo et al., 2009). However, to our best knowledge, results from systematic investigation have never been presented.

Although it is common knowledge that adsorption is surface-dependent, the effect of surfaces on the variation in the intermediates formed from degradation by heterogeneous photocatalysis has not been thoroughly investigated. The present work provides evidence that the adsorption configuration of the compound undergoing degradation on the surface of the catalyst regulates the degradation pathway. Zinc oxide (ZnO) was chosen as the catalyst because it can be synthesized with control of the dominating surface on the particles. A hexagonal crystal of wurtzite ZnO consists of two main sets of surfaces: (i) zinc-terminated (0001) and oxygen-terminated ($000\bar{1}$) polar surfaces located at the top and bottom planes of the crystal, and (ii) mixed-terminated ($10\bar{1}0$) non-polar surfaces as the side planes (Woll, 2007). Herein, the adsorption and photocatalytic degradation of diuron on two different types of ZnO particles, i.e., conventional hexagonal ZnO particles with polar surfaces as the dominating planes, and ZnO nanorods with the mixed-terminated surfaces, were systematically studied. Molecular calculations were also performed to support the experimental findings and to investigate mechanistically how the adsorption configurations affect not only the reaction kinetics, but also the degradation pathway. Finally, the toxicity of the generated intermediates was investigated. It should be noted that 3,4-dichloroaniline (DCA), which shares the same molecular structure as the aromatic part of diuron, was included in the studies to elucidate the effect of molecular structure on the adsorption and photocatalytic degradation of diuron.

## 1. Materials and methods

### 1.1. Synthesis of ZnO

Conventional ZnO powder was synthesized via the sol–gel technique. The procedure was an adaptation from the previous report (Tian et al., 2009). A mixture containing ethanol, diethanolamine, hydrochloric acid, and deionized water in amounts of 5, 1.58, 0.18, and 0.25 mL, respectively, was slowly dropped into a solution of zinc acetate (3.29 g) in 20 mL of deionized water. The mixture was stirred for 2 hr and was aged without stirring for 24 hr. After being dried at 80°C overnight, the mixture transformed into a gel. The gel was aged further for 3 days before being calcined at 500°C for 2 hr to obtain ZnO powder.

In contrast, ZnO nanorods were synthesized via the hydrothermal method modified from that of the previous report (Liu and Zeng, 2003). A precursor solution was prepared from 1.1 g of zinc acetate in 4 mL of deionized water and 6 mL of 8 mol/L sodium hydroxide aqueous solution. Then, 2 mL of the precursor solution was mixed with 5 mL of polyethylene glycol and 20 mL of ethanol. The mixture was heated at 140°C for 1 hr under autogenous pressure in a Teflon-lined autoclave. The precipitate was washed with ethanol and deionized water before being dried at 60°C overnight.

### 1.2. Adsorption studies

Aqueous solutions of diuron and DCA were separately prepared with concentrations in the range of 0–25 mg/L. Adsorption experiments were performed by immersing the catalyst into the solution, of which the temperature was controlled to be 25 ± 2°C. The catalyst content was 1 g/L of the solution. The system was kept in the dark. After 6 hr, which was experimentally determined to be sufficient to reach adsorption equilibrium, the concentration of the solution

was determined by reverse-phase high-performance liquid chromatography (HPLC, Class 10VP, Shimadzu, Japan) (Khongthon et al., 2016). Two separated sets of experiments were conducted, in which data for each concentration was collected in triplicate.

The adsorption processes of diuron and DCA on different surfaces of ZnO were also simulated using density functional theory calculations in the Dmol$^3$ program in the Materials Studio 6.0 package. Each simulation modeled one molecule of either diuron or DCA on 1 layer of a (6 unit cell × 6 unit cell) ZnO surface. The generalized gradient approximation (GGA) with the Perdew-Wang 1991 (PW91) functional was used. A set of polarization functions (DNP) was set up as the basis set with the cutoff radius of 4.4 Å. The electron basis set was used for all elements except Zn, which was treated by an effective core potential. The maximum energy change, the maximum force, and the maximum displacement were set at $1 \times 10^{-5}$ Eh, $2 \times 10^{-3}$ Eh/Å, and $5 \times 10^{-3}$ Å, respectively. The effect of water as a solvent was incorporated in the simulation via the conductor-like screening model (COSMO). The adsorption energy on the surface was calculated as the difference between the energies of the system before and after adsorption. Moreover, using the same setup, the charge distributions on diuron and DCA molecules were also calculated and visualized.

### 1.3. Photocatalytic degradation

The photocatalytic degradation was studied in a microreactor, allowing us to neglect mass transfer resistance for the transport of the compound undergoing degradation to the surface of the catalyst (Khongthon et al., 2016). Furthermore, the residence time within the reactor could be easily controlled, enabling the sequence of intermediates formed from the degradation to be identified. The microreactor was fabricated in a plate-like manner. A piece of glass that had been coated by 6.8 mg of the catalyst via spin-coating was assembled with another piece of glass into which inlet and outlet streams had been drilled. A Teflon sheet with a 0.8 cm × 4.8 cm opening was placed between the pieces of glass, forming a channel. The height of the channel was determined by the thickness of the Teflon sheet (250 μm). The microreactor assembly was then mounted in a stainless-steel housing. The schematic diagram of the photocatalytic set-up is shown in the supplementary information.

A 10 mg/L aqueous solution of either diuron or DCA was constantly supplied into the microreactor via a syringe pump for 1 hr prior to the irradiation to ensure complete adsorption of the compound undergoing degradation onto the catalyst. Then, the reactor was irradiated with light from a 40-W mercury lamp (F40T12/BL, Philips, Netherlands), with an emission spectrum in the wavelength range of 350–410 nm, to initiate the reaction. The power flux at the location of the reactor was found to be $3.18 \times 10^{-6}$ W/cm$^2$, measured by an ILT1700 research radiometer (ILT1700, International Light Technologies, USA) with GaAsP ultraviolet detector (SED005, International Light Technologies, USA). The flow rate was controlled to correspond to the desired residence time in the range of 1–15 min. The concentration of the compound undergoing degradation was monitored at the outlet by HPLC. After reaching a steady state, a sample was collected for identification of the intermediates via liquid chromatography equipped with tandem mass spectroscopy (LC–MS/MS, LCQ Advantage, Thermo Finnigan, USA). The experiments were repeated three times. It should be noted that, according to a preliminary test using inductively coupled plasma optical emission spectroscopy (ICP-OES, Optima7000DV, PerkinElmer, USA), less than 0.5% of the catalyst detached from the reactor throughout the whole period of the experiment.

### 1.4. Toxicity tests

In this work, phytotoxicity and cytogenotoxicity were used as representatives for ecotoxicity of the degradation intermediates (Gyuricza et al., 2010; Souza et al., 2013). They were assessed before and after the treatment. In the phytotoxicity test, four surface-sterilized seeds of mung bean (*Vigna radiate*) were placed on a Petri dish lined with a filter paper that had been soaked with 2 mL of the solution to be tested. The dish was held in a controlled environment at 28°C and 90% relative humidity in the dark for 72 hr. The level of phytotoxicity was inferred from the inhibition of seeding, i.e., the sprouting length.

The cytogenotoxicity was evaluated using the chromosome aberration test with *Allium cepa* (Silambarasan and Vangnai, 2016). Bulbs of *A. cepa* were kept in water in the dark for 72 hr, after removal of their outer scales and dried roots, to promote root development. The roots, which were approximately 15 mm in length, were then exposed to the solution to be tested for 3 hr. The root tips were cut, placed on a glass slide, fixed in Carnoy's solution for 90 min, hydrolyzed in 1 mol/L hydrochloric acid for 10 min, washed, and subsequently stained with 1% aceto-orcein for 5 min. Cell division and cytogenetical abnormalities were observed under a light microscope. The mitotic index (MI) and aberrational cells-to-dividing cells ratio (ADR) were calculated from the following equations.

$$\mathrm{MI} = \frac{N_{dc}}{N_{tc}} \times 100\% \quad (1)$$

$$\mathrm{ADR} = \frac{N_{cab}}{N_{dc}} \times 100\% \quad (2)$$

where, $N_{dc}$, $N_{tc}$, and $N_{cab}$ denote the number of dividing cells, the number of total cells, and the number of chromosomal aberrations cells, respectively.

## 2. Results and discussion

### 2.1. Characteristics of ZnO catalysts

Although detailed characteristics of both catalysts can be found elsewhere (Meephon et al., 2018), the key properties can be summarized as follows. According to X-ray diffraction analyses (XRD, AXS D8, Bruker, Germany) (Appendix A Fig. S2), both catalysts are ZnO in the wurtzite phase without contamination from other crystalline phases. Wurtzite is the thermodynamically stable phase of ZnO at atmospheric pressure, which is stable even after calcination at 1000°C (Li and Haneda, 2003;

Parra and Haque, 2014). The nitrogen adsorption/desorption isotherms of both ZnO catalysts (Appendix A Fig. S3) are Type III in the International Union of Pure and Applied Chemistry (IUPAC) classification, which indicates that they are nonporous. A low-resolution scan of X-ray photoelectron spectroscopy (XPS, DLD, Kratos, Japan) showed that the catalysts contain only zinc and oxygen without contamination from other species, while the high-resolution scan of O1s revealed three states of oxygen, i.e., oxygen in hydroxyl groups, oxygen vacancies, and oxygen in the ZnO lattice, located at the binding energy of 532.2, 531.0, and 530.0 eV, respectively (Appendix A Fig. S4). The content of oxygen vacancies and oxygen in the hydroxyl group on the surface of the ZnO nanorods is only 4.5% and 3.3% higher than that of the ZnO powder, respectively. Hence, both catalysts are considered having similar surface compositions regardless of the fact that the ZnO nanorods were prepared without calcination. The optical bandgaps of both these catalysts, calculated from Tauc plots measured by reflective UV/Visible spectroscopy (Carry5000, Agilent technologies, USA), are the same, i.e., 3.1 eV.

Despite the similarity in the above properties, the scanning electron microscopy (SEM, JSM-7610F, JEOL, Japan) micrographs in Fig. 1 show that the morphologies of the ZnO catalysts synthesized by the two techniques are significantly different. The conventional ZnO particles obtained from the sol–gel technique are micron-sized with low aspect ratio. The hexagonal plane, which is either the (0001) or (000$\bar{1}$) surface, is clearly visible (Fig. 1a). Selected-area electron diffraction (SAED) pattern confirms that the particles are indeed single crystals, which is also consistent with the uniform lattice fringes shown in the high-resolution transmission electron micrograph (HR-TEM, JEM-2100, JEOL, Japan). The inter-planar spacing of the lattice fringes for the conventional particles in Fig. 1a is 2.81 Å, which perfectly agrees with the *d*-spacing for (10$\bar{1}$0) planes calculated from experimental XRD data. Furthermore, since the XRD peaks of the conventional particles align perfectly with those of the standard reference data (i.e., JCPDS 36-1451, Appendix A Fig. S2), it suggests that the synthesized ZnO has the same crystal structure as the standard ZnO, e.g., the angle between (0001) and (10$\bar{1}$0) planes of 90° (Kaneti et al., 2013).

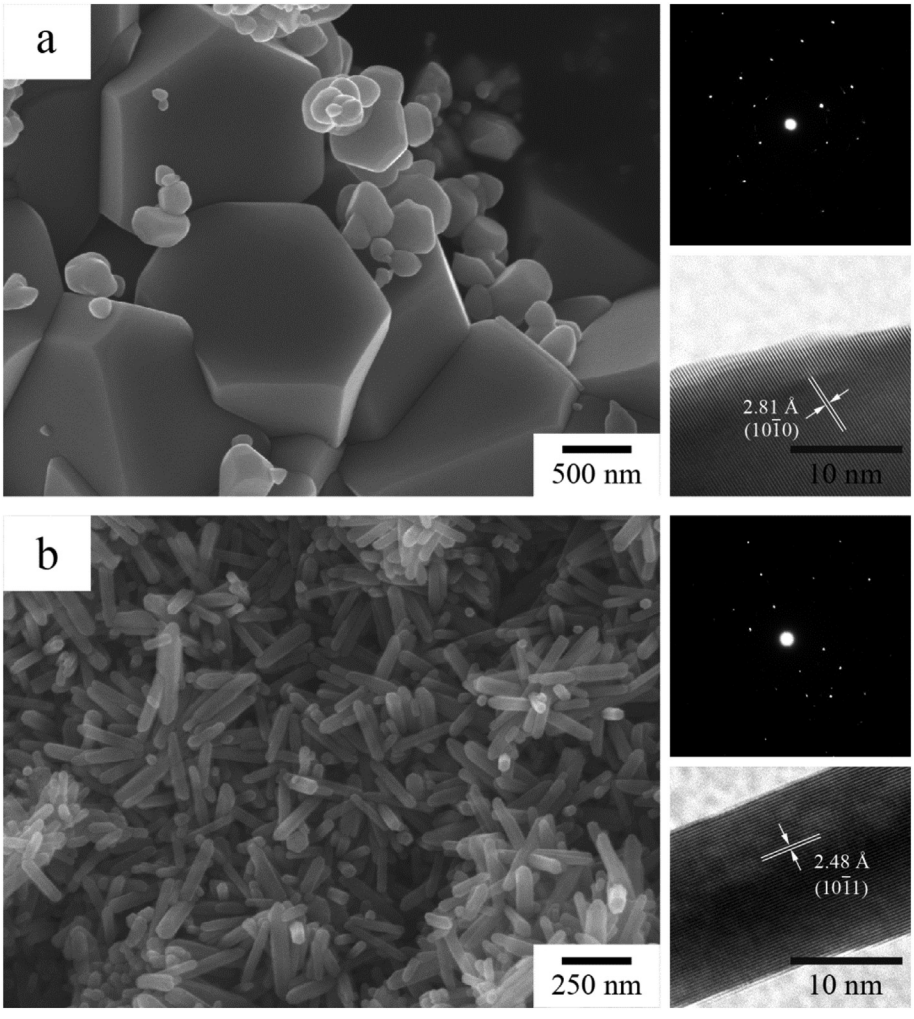


**Fig. 1 – Scanning electron microscopy (SEM) micrograph, high-resolution transmission electron microscopy (HR-TEM) micrograph and selected-area electron diffraction (SAED) pattern of ZnO synthesized by (a) sol–gel and (b) hydrothermal techniques.**

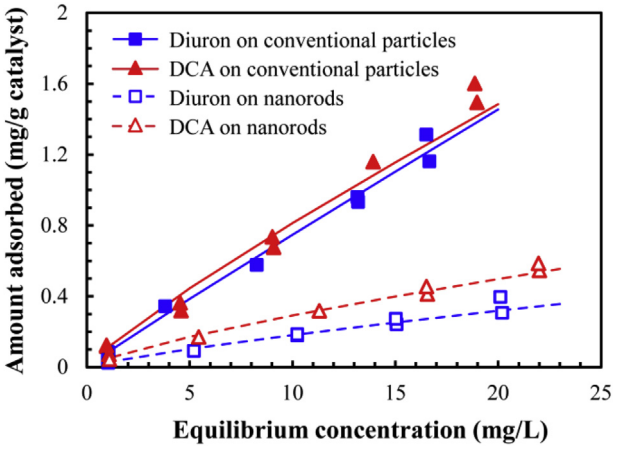


**Fig. 2 – Freundlich adsorption isotherms of diuron and 3,4-dichloroaniline (DCA) on conventional ZnO particles and on ZnO nanorods.**

The ZnO synthesized via the hydrothermal technique is composed of hexagonal nanorods with high aspect ratio (Fig. 1b), of which the dominating exposed plane is the $(10\bar{1}0)$ surface. The length of the rods is in the range of 200–400 nm, while the diameter is about 50 nm. Because of the much smaller particle size of the nanorods, their specific surface area, as measured by nitrogen adsorption using a Brunauer–Emmett–Teller (BET) analyzer (Mini II, Belsorp, Japan), is much higher than that of the conventional particles, i.e., 17 versus 1.4 $m^2/g$. The HR-TEM and SAED indicate that the nanorods are also single-crystalline, which is consistent with the previous report (Liu and Zeng, 2003). The measured inter-planar spacing of the lattice fringes observed in the HR-TEM micrograph in Fig. 1b, i.e., 2.48 Å, agrees with the *d*-spacing for $(10\bar{1}1)$ planes of the JCPDS 36-1451 standard reference data. It should be noted that the XRD pattern of the ZnO nanorods also matches that of the standard reference data as well. Hence, it could be concluded that the ZnO synthesized by both techniques share the same crystal structure and lattice parameters. The major difference between these catalysts is their exposed surfaces. The main exposed surfaces of the nanorods are the mixed-terminated $(10\bar{1}0)$ nonpolar surfaces, while that of the conventional ZnO particles are polar surfaces (i.e., (0001) and $(000\bar{1})$). The area of the nonpolar surface of the nanorods, approximated based on SEM micrographs, is about 18.6 times larger than that of the polar surfaces on top and bottom planes of the nanorods. On the other hand, for the conventional ZnO particles, their polar surface area is about 3.3 times larger than that of the nonpolar surface.

### 2.2. Adsorption of diuron and DCA on catalysts

Experimental data for the adsorption of diuron and DCA on both types of ZnO catalyst are shown in Fig. 2. The Freundlich model (Eq. (3)), which has previously been shown valid for the adsorption of some organic compounds on solid surfaces (Foo and Hameed, 2010), was found to represent the adsorption data well. It should be noted that the Langmuir adsorption model failed to fit the experimental data (Appendix A. Supplementary data) partly because of the limited range of concentration in which the adsorbent is not saturated. However, the experiment was restricted by low solubility of diuron in water, i.e., 35.6 mg/L (Malato et al., 2002). With such low concentration, the adsorption data approach linear form. The fitted Freundlich parameters are presented in Table 1. The values of the Freundlich parameter relating to adsorption intensity ($1/n$) show that both diuron and DCA adsorb on both catalysts by physical adsorption (Hameed et al., 2007; Sivakumar and Palanisamy, 2009), which is consistent with the Fourier transform infrared spectroscopy (FTIR, 6700, Nicolet, USA) results that no signal corresponding to a new bond between the adsorbates and the catalysts was detected after the adsorption experiment was performed. The adsorption intensities show unambiguously that both diuron and DCA adsorb more strongly on the conventional ZnO particles than on the ZnO nanorods even though the nanorods show a slightly higher signal corresponding to oxygen vacancies in the XPS analysis. Hence, although the oxygen vacancies may potentially act as strong adsorption sites, their effects are outweighed by the adsorption on regular surfaces and will not be considered as the factor responsible for the difference in the results from two catalysts. It should be noted that zeta-potential of the conventional ZnO particles and the ZnO nanorods, measured in deionized water (pH of 6.8 as same as both diuron and DCA solutions) using Zetasizer (Nanoseries S4700, Malvern, UK) is −30 and −14 mV, respectively.

$$q_e = K_f C_e^{1/n} \tag{3}$$

where, $q_e$ (mg/mg catalyst) is the amount of compound adsorbed on the adsorbent, $C_e$ (mg/L) is equilibrium concentration in the solution, and $K_f$ and $n$ are fitted parameters.

Fig. 2 clearly illustrates that greater amounts of both adsorbates were adsorbed on the conventional ZnO particles than on the ZnO nanorods, even though the surface area of the former is one order of magnitude lower than the latter, which might be expected to produce the opposite result. The same conclusion was achieved even when the adsorption analysis was done on the basis of per unit area (Appendix A Fig. S14). The fitted parameter relating to adsorption capacity ($K_f$) (Sivakumar and Palanisamy, 2009) for adsorption on the conventional ZnO particles is about twice the value for the nanorods. This issue will be discussed below in terms of the molecular calculations. Comparing the two adsorbates, it is found that $K_f$ for DCA adsorption is significantly higher than that of diuron because of the much smaller molecular size of DCA, which allows more DCA molecules to be accommodated on the surface than diuron.

To further understand the adsorption of diuron and DCA onto various surfaces of ZnO, molecular calculations were performed. For each surface, several initial positions and orientations of the adsorbate molecule were tested to obtain the most stable adsorption configuration. The associated adsorption energy for each case is shown in Table 2, while the optimized molecular configurations for the adsorption of

**Table 1 – Fitted parameters for Freundlich adsorption model.**

| Parameter | Adsorption of diuron | | Adsorption of DCA | |
|---|---|---|---|---|
| | On conventional ZnO particles | On ZnO nanorods | On conventional ZnO particles | On ZnO nanorods |
| $K_f$ ($L^{1/n}.mg^{(1-1/n)}/g_{ZnO}$) | 0.082 | 0.028 | 0.110 | 0.049 |
| $1/n$ | 0.959 | 0.815 | 0.868 | 0.772 |
| $R^2_{fitting}$ | 0.992 | 0.963 | 0.983 | 0.978 |
| $R^2_{data}$ | 0.986 | 0.947 | 0.975 | 0.987 |

$K_f$: adsorption capacity; $R^2_{fitting}$: $R^2$ for the linearized plot to find Freundlich parameters; $R^2_{data}$: $R^2$ for the comparison between the fitted model and the experimental data.

diuron and DCA on the surfaces are shown in Figs. 3 and 4, respectively. The calculated energies support the experimental finding that adsorption on the mixed-terminated nonpolar surface of ZnO is less favorable than that on polar surfaces.

According to the adsorption configurations in Figs. 3 and 4, the observation that negatively charged part of the molecule, such as methoxy oxygen of diuron, approaches positively charged atom on the surface (i.e., zinc atom), while chlorine atoms are repelled by negatively charged surface atom (i.e., oxygen atom) suggested that the interactions between either diuron or DCA and the surfaces of ZnO are electrostatic. Hence, the charge distributions within molecules of diuron and DCA were studied. The potential maps are shown in Fig. 5. For diuron, electrons in the aliphatic part of the molecule are localized at the oxygen and nitrogen atoms. The aromatic part is relatively electron-rich, i.e., with electron density delocalized in the ring and localized around chlorine atoms. The charge distribution of DCA is mostly similar to that of diuron, especially in the aromatic part. The most electron-rich location in DCA is its nitrogen atom. As expected, all hydrogen atoms in both diuron and DCA are positively charged.

According to the simulation of adsorption on the mixed-terminated surface of ZnO (Fig. 3a), diuron adopts a bent conformation so that the most negatively charged part of the molecule, i.e., the amide oxygen and nitrogen attached to the aromatic ring, can approach positively charged zinc atoms on the surface at distances of 2.2 and 2.6 Å, respectively. At the same time, the hydrogen atoms in both methyl groups are attracted by the oxygen atoms of ZnO at distances of 2.4 Å. This C–H···O interaction is specifically considered as a weak hydrogen bond, although it is generally classified as strong electrostatic interaction (Steiner, 1997). Nevertheless, in similar manner as other electrostatic interaction, it could not be detected by FTIR (Steiner, 2002). Being restricted by the size of the molecule, the two chlorine atoms on the aromatic end of diuron are located near oxygen atoms on the surface and thereby are repelled from the surface. The adsorption configuration of DCA onto the mixed-terminated surface (Fig. 4a) is similar to that of diuron. The repulsive forces between the chlorine atoms and surface oxygen atoms cause the DCA molecule to tilt, lifting the chlorines away from the surface. Meanwhile, the hydrogen atoms in the amine functional group, which are positively charged because of electron withdrawal by the nitrogen atom, are attracted to surface oxygen atoms, forming weak hydrogen bonds. Having fewer functional groups attracted to the surface, the adsorption energy of DCA is lower than that of diuron by ca. 3.0 kcal/mol. On the other hand, because of the small molecular size of DCA, the projected area of the surface that is occupied by each DCA molecule is much smaller than that for diuron (i.e., 80.5 versus 112.9 $Å^2$). This causes DCA to have a higher adsorption capacity than diuron, which is consistent with the values of $K_f$ from the adsorption experiments in Table 1. In fact, the adsorption capacity should be defined with respect to the ratio between the total surface area of the catalyst and the projected occupied area per molecule. If this ratio for DCA is divided by the ratio for diuron adsorption on the same catalyst, the result is the ratio between the projected area occupied by diuron and that by DCA. The obtained value, therefore, represents the ratio of the adsorption capacity of DCA to that of diuron. It should be noted that the ratio between the experimental $q_e$ of DCA and that of diuron (i.e., 1.58) corresponds well with the ratio of the calculated area occupied by diuron to that of DCA (i.e., 1.40). This implies the validity of the simulation.

**Table 2 – Calculated adsorption energy for adsorption of diuron and DCA on each surface of ZnO.**

| Adsorbate | Adsorption energy (kcal/mol) | | |
|---|---|---|---|
| | Mixed-terminated surface | Zinc-terminated surface | Oxygen-terminated surface |
| Diuron | −31.89 | −38.17 | −42.86 |
| DCA | −28.93 | −34.48 | −39.91 |

On the zinc-terminated surface (Figs. 3b and 4b), both compounds adsorb in a planar configuration, i.e., the aromatic ring is parallel to the surface. Because the surface is uniformly composed of positively charged zinc atoms, both ends of the diuron and DCA molecules, which are electron-rich, are attracted to the surface simultaneously. For DCA, two chlorine atoms and a nitrogen atom are located almost on top of zinc atoms on the surface (at distances of 2.7 and 2.3 Å, respectively). The amine functional group adopts a bent conformation such that the nitrogen atom, which is the most electron-rich part of the molecule, leans toward the surface as a result of attraction, while two hydrogen atoms are pushed upward to minimize repulsion with the surface. However, for diuron adsorption, the aliphatic chain of diuron is twisted such that the methoxy oxygen tilts toward the surface while both methyl groups are repelled away from the surface. The distance between the oxygen atom in diuron and the closest zinc atom on the surface is 2.2 Å, which is approximately the same as the corresponding distance for adsorption on the mixed-terminated surface. The energies of adsorption on the zinc-terminated surface are significantly

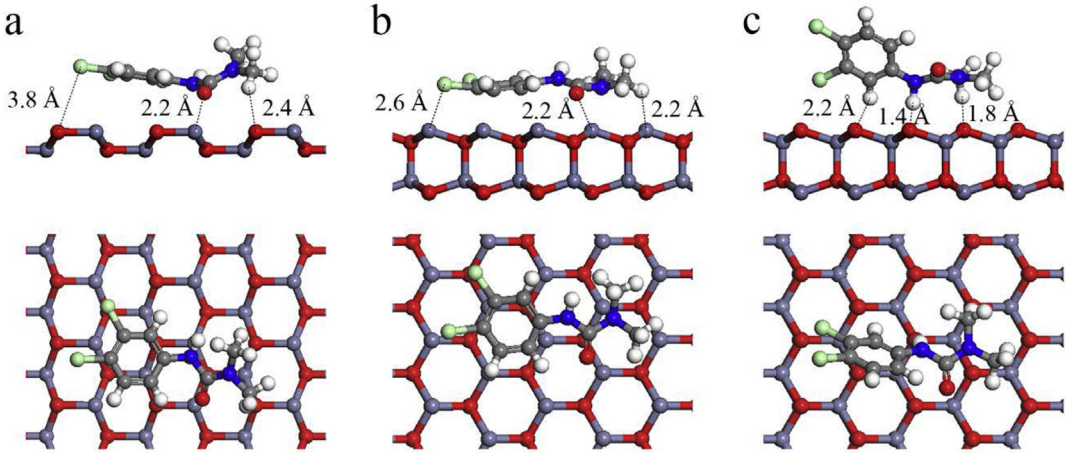


**Fig. 3 – Optimized models for adsorption of diuron on (a) mixed-terminated ($10\bar{1}0$) surface, (b) zinc-terminated (0001) surface, and (c) oxygen-terminated ($000\bar{1}$) surface.**

higher than those on the mixed-terminated surface (by 6.3 and 5.6 kcal/mol for diuron and DCA, respectively), which is consistent with reports that polar surfaces have higher surface energy than nonpolar surfaces (Kornherr et al., 2004; Kornherr et al., 2006).

On the oxygen-terminated surface, the molecular configurations of surface-adsorbed diuron and DCA are completely different from each other (see Figs. 3c and 4c). Diuron tilts almost perpendicularly so that the electron-rich amide oxygen moves away from the negatively charged oxygen on the surface, while positively charged hydrogen atoms turn toward the surface. The repulsion between the surface and the delocalized electrons in the aromatic ring is also minimized. Tilting allows hydrogen atoms in the methyl group and the aromatic ring to form C–H···O interactions with the surface, which are stronger than the conventional attraction between opposite charges (Steiner, 1997). Hence, the adsorption energy on the oxygen-terminated surface (–42.86 kcal/mol) is much more negative (i.e., more favorable) than that on the zinc-terminated surface (–38.17 kcal/mol). However, for DCA, the hydrogen atoms in the amine group are positioned toward the surface because they are more positively charged than the aromatic hydrogens because of the high electronegativity of nitrogen. Although the adsorption configuration of DCA on the oxygen-terminated surface is similar to that on the mixed-terminated surface, the adsorption energy on the former is significantly more favorable (by 11.0 kcal/mol) because the aromatic ring in DCA on the mixed-terminated surface is subjected to repulsive interactions between the two chlorine atoms and the surface oxygen atoms. This repulsion is unavoidable as long as the delocalized electrons in the ring are attracted to the zinc atoms on the surface. For DCA on the oxygen-terminated surface, such repulsion is minimized by the substantial tilting of the ring away from the surface.

The adsorption experiments showed that the adsorption capacity of DCA on the conventional ZnO particles is higher than that of diuron in the same manner as that observed on

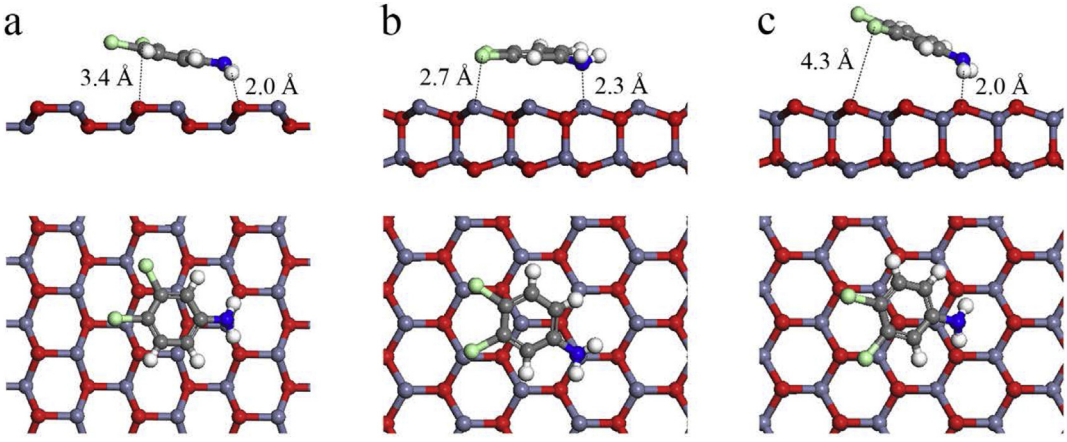


**Fig. 4 – Optimized models for adsorption of DCA on (a) mixed-terminated ($10\bar{1}0$) surface, (b) zinc-terminated (0001) surface, and (c) oxygen-terminated ($000\bar{1}$) surface.**

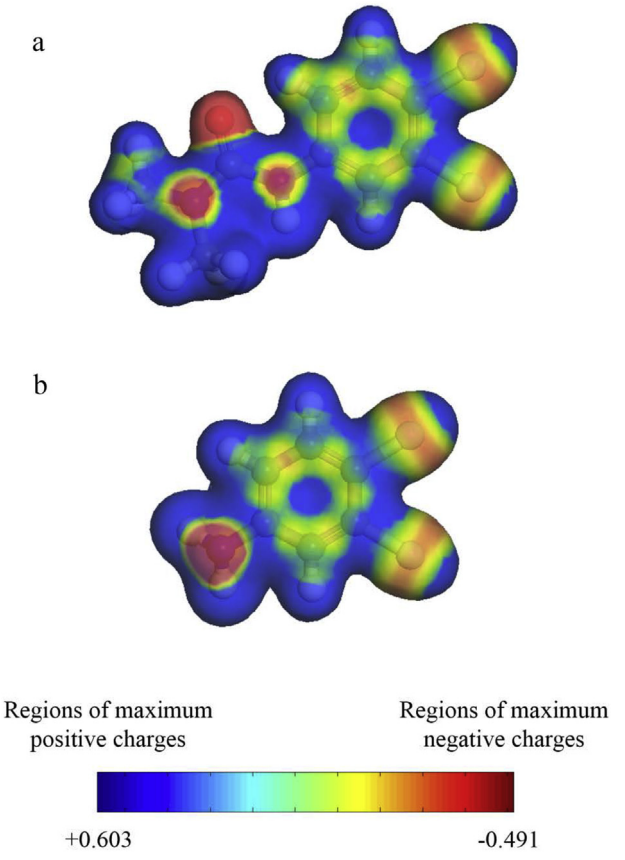


**Fig. 5 – Charge distribution of (a) diuron and (b) DCA.**

the ZnO nanorods because of the small molecular size of DCA. However, for the case of the conventional ZnO particles, the ratio of the calculated area occupied by diuron to that of DCA could not be directly related to the experimental $q_e$ ratio because the distributions of the adsorbate molecules on zinc- and oxygen-terminated surfaces are not known.

If the atom on the surface that is closest to the adsorbate molecule is defined as the adsorption site, Figs. 3 and 4 show that, on the mixed-terminated surface, zinc is the adsorption site for diuron, while oxygen is the adsorption site for DCA. As stated previously, several initial positions of the adsorbate molecule were tested and the adsorption of diuron on oxygen and adsorption of DCA on zinc were found to be much less stable than the configurations reported in Figs. 3 and 4. In other words, only half of the surface atoms of the mixed-terminated surface are sites for stable adsorption. On the other hand, for the polar surfaces, all atoms can serve as adsorption sites. Furthermore, the adsorbate molecules that are already adsorbed on the surface will exert steric effects hindering adsorption on nearby sites. This steric effect will more severely reduce the adsorption capacity on the mixed-terminated surface, where not all atoms are potential adsorption sites, especially for diuron molecules, which are much larger than DCA. These factors contribute to the result that the adsorption capacity on the conventional ZnO particles is much higher than that on the nanorods.

Last, the simulation results confirm the experimental finding that the adsorption of either diuron or DCA on any surface of ZnO is still physical in nature because the distances between the adsorbate molecules and the adsorption sites are too long to be considered as chemical bonds (Pacchioni, 1993).

### 2.3. Photocatalytic degradation

In the heterogeneous photocatalysis, the process is initiated by excitation of the catalyst by light to generate photoinduced electrons ($e^-$) and holes ($h^+$). The photocatalytic oxidation of an organic compound adsorbed on a catalyst can in principle take place either via direct oxidation by photogenerated holes or indirect oxidation by generated radicals (e.g., hydroxyl or superoxide radicals). For ZnO, the potential of the electrons in the conduction band (−0.2 eV (Yu et al., 2015)) is not enough to reduce $O_2$ to superoxide radical since the potential of $\bullet O_2^-/O_2$ is −0.33 eV (Li et al., 2019). On the other hand, because the potential of the valence band, i.e., +3.0 eV, is more positive than that of $OH\bullet/OH^-$ (+2.27 eV) (Yu et al., 2015), the holes are likely to react with plentiful surrounding $OH^-$ in aqueous solution to form hydroxyl radicals (Li et al., 2018; Wang et al., 2018) and subsequently induce indirect oxidation with the adsorbed organic compound. More importantly, it has been reported that chemisorption is a prerequisite for direct oxidation while physisorption is favorable for indirect oxidation (Montoya et al., 2014). Because it was shown in the previous section, via both the experimental and calculated results, that both diuron and DCA attach to conventional ZnO particles and ZnO nanorods via physical adsorption, it is suggested that the photocatalytic degradation in this work occurs via indirect oxidation. Furthermore, although the radicals can in principle diffuse into the bulk liquid and react with the pollutant there, this homogeneous reaction is considered negligible compared with oxidation on the surface (Turchi and Ollis, 1990; Lawless et al., 1991).

The results for the photocatalytic degradation of diuron using the two different ZnO catalysts are shown in Fig. 6a. After 15 min of residence time, the concentration of diuron in the solution was decreased from 10 to 1.85 and 1.75 mg/L when the conventional ZnO particles and ZnO nanorods were used as the catalyst, respectively. The experimental data obtained at several residence times are used to fit the steady-state mathematical model of the degradation. It has been reported that the photocatalytic degradation rate of diuron on zinc oxide can be described by the pseudo-first order kinetics (Fenoll et al., 2013b). The reaction rate constant was simply determined from the slope of the ln ($C_{in}/C_{out}$) versus residence time graph, where $C_{in}$ and $C_{out}$ are concentrations at inlet and outlet of the reactor, respectively. The fitted models are shown as lines in Fig. 6 and the fitted parameters are shown in Table 3. It should be noted that the $R^2$ for the fitting of the model to the experimental data are not exceptionally high because detailed transport phenomena within the microreactor was not included (Khongthon et al., 2016). Nevertheless, the reaction rate constants obtained are in the same range as reported in literature (Malato et al., 2003; Fenoll et al., 2013b), although the intensity of the light used in this work is approximately three orders of magnitude lower. This is one of the advantages of a microreactor. Although fresh catalyst was used for every experiment, the XRD characterization of the used catalysts confirmed that both crystal

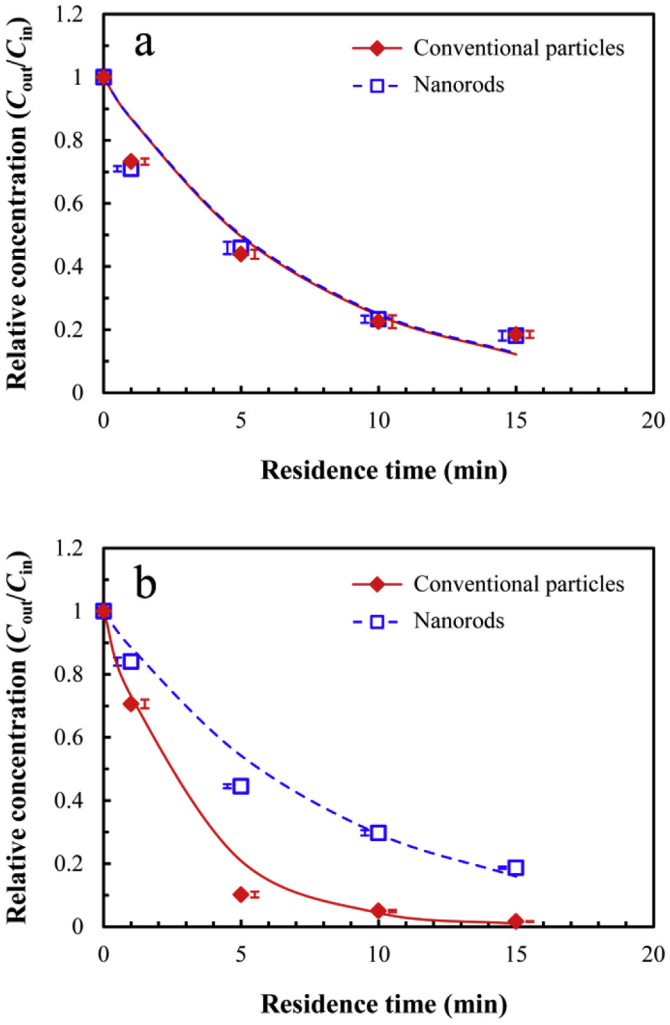


**Fig. 6 – Fitting of the pseudo-first order kinetic model to the experimental results on the photocatalytic degradation of (a) diuron and (b) DCA solutions using conventional ZnO particles and ZnO nanorods. The error bars are intentionally shifted for clarity of the plot.**

structure and lattice parameters of the catalysts were not changed throughout the whole degradation experiment.

The diuron degradation kinetics are not significantly different between the two catalysts, even though the experimental adsorption results showed that the adsorption capacity of diuron on the conventional particles was about 4 times larger than that on the nanorods (Fig. 2). Because the surface area of the nanorods is one order of magnitude larger than that of the conventional particles, diuron molecules on the surface of the nanorods are expected to be much more dispersed than those on the conventional particles. This lowers probability for diuron on the nanorods to be attacked by the hydroxyl radicals. It should be noted that both surface area and the amount of diuron adsorbing on the surface play an intertwining effect on the photocatalytic activity in this case. Therefore, the degradation of diuron on ZnO should not be evaluated based only on BET surface area, which is consistent with the report in literature (Wang et al., 2005). On the other hand, considering the adsorption configuration, the aliphatic side of diuron adsorbs onto the mixed-terminated surface of the nanorods, while the aromatic part is repelled away from the surface. Hence, the oxidation of diuron by a hydroxyl radical should occur at the aliphatic moiety. This is supported by the structures of diuron degradation intermediates that show sign of oxidation only on their aliphatic moiety (more detail in Section 2.4). For the polar surfaces, however, the hydroxyl radical can attack the molecule of diuron on either the aliphatic or aromatic side because both sides adsorb onto the surfaces at the same time. Because the aromatic ring is much more stable than the aliphatic part of the molecule, as witnessed from the widely reported observation that ring-opening is the last step of the degradation pathway (Farre et al., 2007; Katsumata et al., 2009; Chusaksri et al., 2011), the attack on the aromatic side is not as effective toward the degradation of diuron as that on the aliphatic side. The actual rate of diuron degradation on the surface of the conventional particles is, therefore, slower than on the nanorods. This argument is supported by the results of the photocatalytic degradation of DCA. Because DCA does not have an aliphatic moiety, the hydroxyl radicals will attack its aromatic ring regardless of its adsorption configuration on the surface. Hence, the extent of the degradation of DCA depends mainly on the adsorption capacity. The results in Fig. 6b confirm this conclusion. The extent of DCA degradation on the conventional ZnO particles, which have much higher DCA adsorption capacity, is greater than that on the nanorods.

### 2.4. Diuron degradation intermediates

The outlet stream from the reactor was collected and analyzed by LC–MS/MS to determine the structures of the diuron degradation products. Figs. 7 and 8 report the major intermediates detected at different residence time when the ZnO nanorods and the conventional particles were used as the catalyst, respectively. The use of a microreactor, i.e., a continuous flow reactor, allows better identification of the sequence of intermediates formation than the experiment in a batch reactor. Within 15 min of residence time, the total of 8 reaction intermediates are formed on the ZnO nanorods, while 11 intermediates are generated from the diuron degradation on the conventional ZnO particles. The intermediates formed on these two catalysts are markedly different. Only 5 intermediates are common intermediates. Comparing with the intermediates reported in the previous work on the photocatalytic degradation of diuron on ZnO (Fenoll et al., 2013b), 11 new intermediates were identified in this work. The pathways are inferred from the molecular structures of the intermediates. No intermediate was detected from the photolysis of diuron in the absence of a catalyst, because the extent of degradation was very low, i.e., $C_{out}/C_{in}$ was equal to only 0.98 even after a residence time of 15 min. In the presence of catalysts, intermediates were detected in the experiments with residence time of at least 1 min (but not with shorter residence time). It is therefore assumed that the intermediates detected at the residence time of 1 min were derived from photocatalytic diuron degradation. The concentrations of the detected intermediates could not be measured because of the lack of commercial standard reference

**Table 3 – Fitted kinetic parameters for photocatalytic degradation.**

| Parameter | Degradation of diuron | | Degradation of DCA | |
|---|---|---|---|---|
| | On conventional ZnO particles | On ZnO nanorods | On conventional ZnO particles | On ZnO nanorods |
| $k_{app}$ ($min^{-1}$) | 0.141 | 0.139 | 0.313 | 0.123 |
| $R^2$ | 0.949 | 0.940 | 0.984 | 0.973 |

$k_{app}$: apparent rate constant.

compounds. However, all of the intermediates reported in Figs. 7 and 8 were assumed to have concentrations on the same order of magnitude because their corresponding chromatographic peak heights were similar. All paths shown are therefore major degradation pathways of diuron.

For the degradation on the ZnO nanorods, the first set of intermediates, i.e., 3-(3,4-dichlorophenyl)-1-(hydroxymethyl)-1-methylurea (C1) and 1-(3,4-dichlorophenyl)-3-methylurea (C2), are formed by hydroxylation and demethylation at the methyl group, respectively. Interestingly, these reactions take place at the aliphatic moiety of diuron, which is the part of the molecule adsorbed on the mixed-terminated surface of the nanorods. Nevertheless, the methoxy oxygen, which is the closest part of the adsorbed diuron to the surface, is not attacked by the hydroxyl radical. An attack by hydroxyl radicals involves two steps, i.e., initiation and termination. In the initiation step, a hydroxyl radical transfers its radical character to a part of the adsorbate molecule. Then, the adsorbate radical combines with another hydroxyl radical in the termination step. It has been reported that the initiated adsorbate radical is more stable and more likely to proceed to the termination step when the attack of the hydroxyl radical takes place on either an atom with low electronegativity, such as carbon or hydrogen, or an atom attached to an atom with lone-pair electrons (Gozzo, 2001; Devipriya and Yesodharan, 2005; Yuan et al., 2012). Therefore, for diuron, the attack on the methyl group would produce a more stable adsorbate radical than that on the methoxy oxygen; hence the formation of C1 and C2. It should be noted that there is no sign of an attack by the hydroxyl radical on the aromatic side of diuron

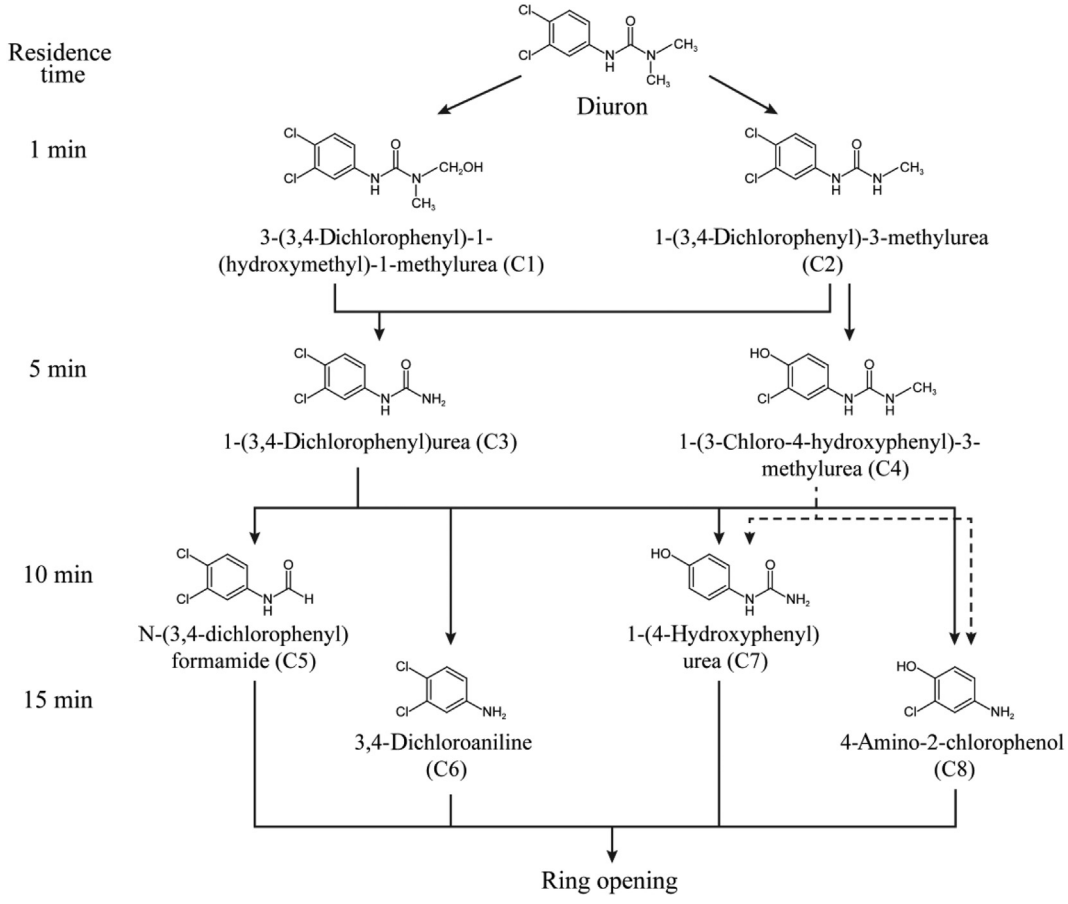


**Fig. 7 – Structures of diuron degradation intermediates identified by liquid chromatography equipped with tandem mass spectroscopy (LC–MS/MS) and proposed degradation pathway of diuron catalyzed by ZnO nanorods.**

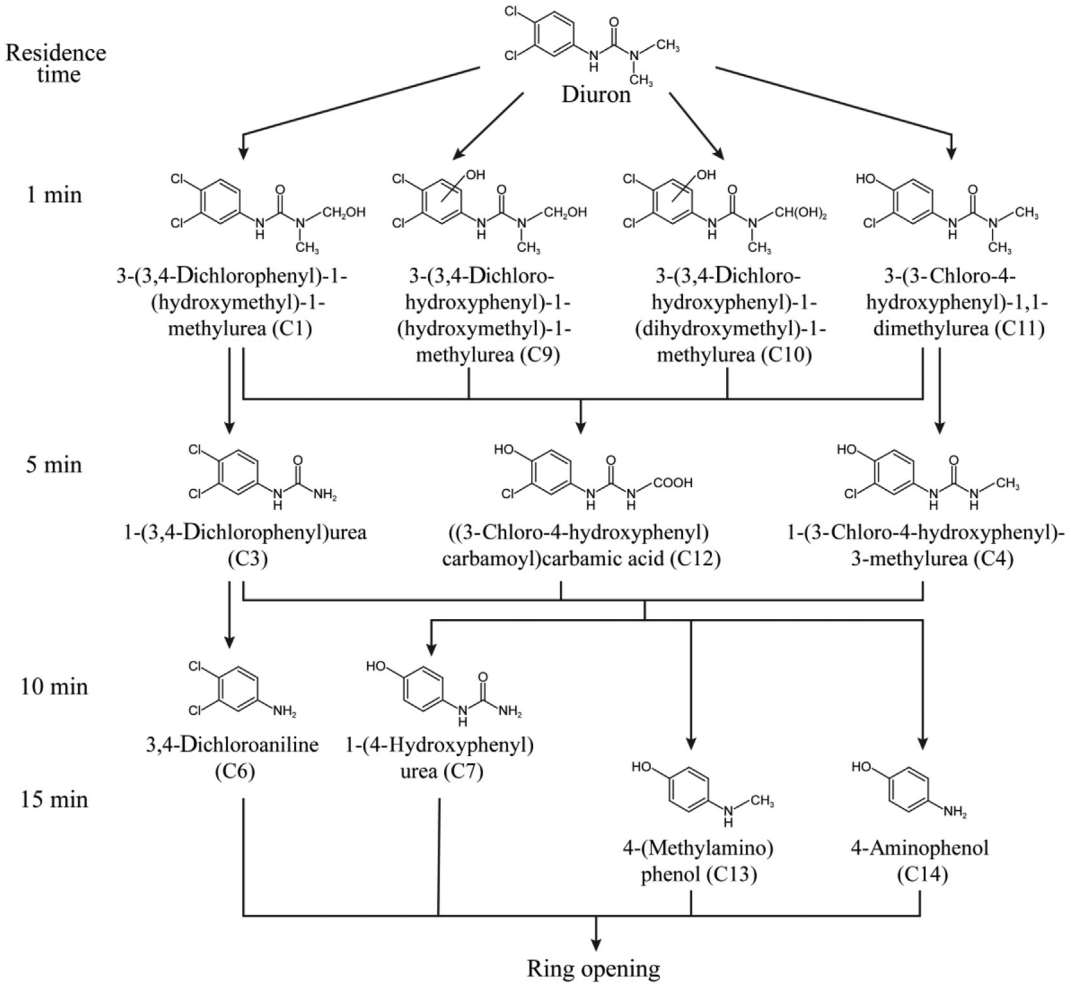


**Fig. 8 – Structures of diuron degradation intermediates identified by liquid chromatography equipped with tandem mass spectroscopy (LC–MS/MS) and proposed degradation pathway of diuron catalyzed by conventional ZnO particles.**

within short residence time because the aromatic ring is lifted away from the surface by the repulsion between chlorine atoms on the ring and oxygen atoms on the surface (Fig. 3). The lengthening distance of the ring from the surface lowers the probability of attack by the hydroxyl radical. However, as the residence time is prolonged, an attack on the aromatic side is eventually witnessed. The fact that DCA (C6) was detected only at long residence time discourages the suggestion from the previous report, which was conducted in a batch reactor, that DCA could be formed via direct hydrolysis of diuron or C2 (Fenoll et al., 2013a).

Despite the similar conversion rates, the degradation pathway on the conventional ZnO particles is markedly different from that on the nanorods. We propose that the difference in pathways is caused by the adsorption configurations of diuron onto the surfaces. As previously discussed, diuron adsorbs in a planar configuration on the zinc-terminated surface, while it turns perpendicularly to the oxygen-terminated surface. Both of these give rise to equal probabilities of attack by the hydroxyl radicals on either the aliphatic or aromatic parts of diuron, hence the formation of both C1 and 3-(3-chloro-4-hydroxyphenyl)-1,1-dimethylurea (C11). Intermediates resulting from diuron being attacked on both sides of the molecule simultaneously, i.e., 3-(3,4-dichloro-hydroxyphenyl)-1-(hydroxymethyl)-1-methylurea (C9) and 3-(3,4-dichloro-hydroxyphenyl)-1-(dihydroxymethyl)-1-methylurea (C10), were also observed during the degradation experiment even within short residence time. By the nature of physical adsorption, these intermediates can easily desorb from the surface. Nevertheless, as the residence time is prolonged, the intermediates re-adsorb and undergo further degradation until mineralization is achieved. The structure of the subsequent intermediates should, therefore, depend on the adsorption characteristics of the products from the prior step in the pathway. It should also be noted that, although the presence of the intermediates may not interfere with diuron adsorption within short residence time because of low concentration of the intermediates due to low conversion of diuron, the accumulated amount of the intermediates would compete with diuron adsorption and may exert interfering effect toward diuron adsorption configuration. Further detailed study is needed.

DCA was detected as one of the intermediates of diuron degradation on both catalysts. Unfortunately, because of the

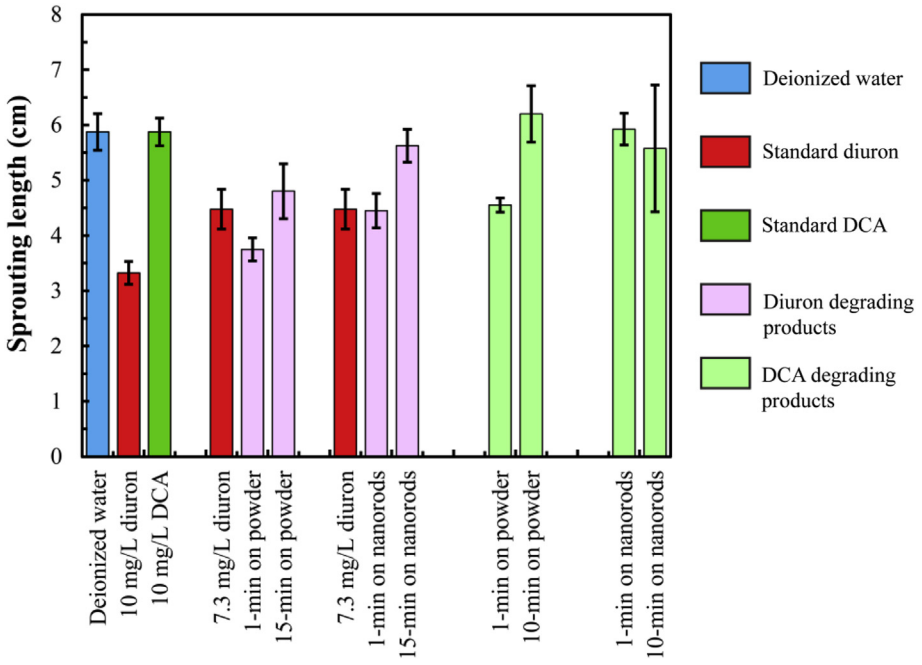


**Fig. 9 – Phytotoxicity assessment of the products of the photocatalytic degradation of diuron and DCA, determined via sprouting length of *Vigna radiate* specimens exposed to the products.**

small molecular size of the DCA degradation intermediates, the analysis via LC–MS/MS failed to reliably identify their structures.

### 2.5. *Toxicity of the degradation products*

This section emphasizes on the importance of pathway shifting toward the abatement of the toxicity because it is the goal of the degradation of toxic pollutants. Both the phytotoxicity and cytogenotoxicity of the degradation products were evaluated in comparison with their parental substrates in this work. In addition to the products of diuron degradation, the products of DCA degradation were also tested for toxicity because DCA is one of the intermediates in the diuron degradation pathway. Other intermediates could not be individually tested because they are not commercially available. Deionized water was used as a negative control.

Fig. 9 shows the sprouting length of *V. radiate* seeds after being exposed to the products of diuron and DCA degradation for the residence time of 1 and 15 min, respectively. The longer the sprouting length, the lower the phytotoxicity is. The phytotoxicity of diuron is clearly indicated by the significant shortening of the sprouts, while DCA at a concentration of 10 mg/L seems to be benign. For diuron, it can be seen that the photocatalytic degradation products generally have lower toxicity than diuron itself. The longer the residence time, the less toxic the products become. Nevertheless, to assess the toxicity of the intermediates (specifically for the degradation using a residence time of 1 min) the degradation product was compared with a diuron-only solution prepared with the same concentration as that of residual diuron in the degradation product (7.3 mg/L). The product degraded by the ZnO nanorods showed roughly the same level of toxicity as the reference diuron, implying that the degradation intermediates C1 and C2 have much lower toxicity than diuron itself. However, when the conventional ZnO particles were used, the degradation product showed higher toxicity than the reference diuron solution. Therefore, at least one of the intermediates, i.e., C9, C10 or C11, probably has potent toxicity, although more specific conclusions cannot be drawn because the exact concentrations of the intermediates are not known. It should be noted that both catalysts achieved roughly the same conversion of diuron. This shows beyond doubt that the intermediates formed from diuron degradation on the ZnO nanorods are less toxic than those generated on the conventional ZnO particles. The product treated on the nanorods for 15 min appears to be almost as benign as pure deionized water.

For the degradation of DCA, a compound that is considered benign in terms of phytotoxicity, the use of the conventional ZnO particles was found to generate initial intermediates that were more toxic than DCA itself, as witnessed from the significant shortening of the sprouts treated with the degradation product obtained after a residence time of 1 min. Only when the residence time was prolonged to 10 min did the product become benign again. However, for the degradation on the nanorods, all of the products appeared to be consistently benign regardless of residence time.

Cytogenotoxicity, which is toxicity toward disruption of chromosome during cell mitosis, was assessed in addition to the phytotoxicity test. The level of cytogenotoxicity is conventionally evaluated through the mitotic index (MI), based on the number of dividing cells (Eq. (1)). The number of

**Table 4 – Mitotic indexes and chromosomal aberration for mitosis of *Allium cepa* exposed to the degradation products.**

| Treatment | MI (%) | Chromosomal aberrations in 500 counted cells | | | | | | ADR |
|---|---|---|---|---|---|---|---|---|
| | | CB | MC | ML | MA | AB | AL | |
| Standard solutions | | | | | | | | |
| Deionized water | 19.70 ± 0.72 | 4.2 ± 0.38 | 1.3 ± 0.15 | 2.0 ± 0.13 | 0.2 ± 0.08 | – | – | 0.0787 ± 0.0037 |
| 10 mg/L diuron solution | 9.45 ± 0.27 | 1.5 ± 0.28 | 4.0 ± 0.31 | 3.5 ± 0.80 | 0.8 ± 0.20 | – | 0.5 ± 0.33 | 0.2174 ± 0.0337 |
| 7.3 mg/L diuron solution | 13.10 ± 0.13 | 6.5 ± 0.36 | 3.0 ± 0.53 | 0.5 ± 0.13 | – | – | 1.0 ± 0.29 | 0.1679 ± 0.0144 |
| 10 mg/L DCA solution | 16.20 ± 0.48 | 4.0 ± 0.80 | 4.5 ± 0.39 | 3.0 ± 0.42 | 1.3 ± 0.36 | – | 2.7 ± 0.58 | 0.1917 ± 0.0216 |
| Degradation of diuron | | | | | | | | |
| 1 min using ZnO powder | 10.30 ± 0.24 | 8.0 ± 0.78 | 1.5 ± 0.13 | 0.2 ± 0.05 | 0.2 ± 0.10 | – | 1.3 ± 0.80 | 0.2189 ± 0.0289 |
| 15 min using ZnO powder | 15.15 ± 0.22 | 5.3 ± 0.27 | 2.3 ± 0.27 | 1.2 ± 0.33 | – | – | 0.7 ± 0.22 | 0.1254 ± 0.0071 |
| 1 min using ZnO nanorods | 11.45 ± 0.10 | 7.8 ± 0.53 | 0.7 ± 0.13 | 1.5 ± 0.45 | – | – | 1.5 ± 0.58 | 0.2008 ± 0.0256 |
| 15 min using ZnO nanorods | 18.90 ± 0.38 | 6.3 ± 0.33 | 0.8 ± 0.27 | 0.3 ± 0.02 | 0.2 ± 0.03 | – | 1.0 ± 0.29 | 0.0900 ± 0.0039 |
| Degradation of DCA | | | | | | | | |
| 1 min using ZnO powder | 13.9 ± 0.17 | 9.0 ± 0.43 | 4.5 ± 0.40 | 0.5 ± 0.41 | 0.5 ± 0.12 | – | 1.0 ± 0.10 | 0.2086 ± 0.0048 |
| 10 min using ZnO powder | 15.15 ± 0.48 | 10.0 ± 0.49 | 1.8 ± 0.48 | 1.5 ± 0.09 | – | – | 1.5 ± 0.26 | 0.1949 ± 0.0087 |
| 1 min using ZnO nanorods | 15.05 ± 0.22 | 6.5 ± 0.14 | 2.5 ± 0.61 | 2.5 ± 0.22 | 0.3 ± 0.03 | – | 1.7 ± 0.34 | 0.1795 ± 0.0103 |
| 10 min using ZnO nanorods | 15.25 ± 0.23 | 10.5 ± 0.33 | 1.2 ± 0.13 | 0.5 ± 0.02 | – | – | 0.8 ± 0.04 | 0.1705 ± 0.0028 |

MI: mitotic index; CB: chromosome breaks; MC: metaphase cluster; ML: metaphase lagging chromosome; MA: metaphase aberrations; AB: anaphase bridge; AL: anaphase lagging chromosome; AI: aberration index; ADR: aberrational cells-to-dividing cells ratio.

cells showing cytogenetical abnormalities is also important, and the aberrational cells-to-dividing cells ratio (ADR) was calculated to determine the fraction of dividing cells that showed abnormalities. Both sets of ratios are given in Table 4. It should be noted that large MI refers to healthy cells division, hence low toxicity. On the other hand, high chromosomal aberrations (i.e., large number for chromosomal defects in each phase of cell mitosis, including chromosome breaks, metaphase cluster, metaphase lagging chromosome, metaphase aberrations, anaphase bridge, and anaphase lagging chromosome) or high ADR reflects high toxicity of the sample toward causing abnormalities in cell divisions.

Diuron is much more toxic than water in terms of inhibition of cell division, and it exerted a significant aberrational effect on the cell mitosis. For the photocatalytic degradation of diuron using the conventional ZnO particles, the toxicity was generally reduced by the treatment, as shown by the increased MI and decreased ADR. However, the intermediates generated within a short period of time caused significant abnormalities in the cell, as seen by comparing the effect of the degradation product with that of the reference diuron solution having the same diuron concentration as the degradation product. This result is consistent with the results of the phytotoxicity test. For the degradation on the ZnO nanorods, the degradation product using 1 min residence time also showed a higher level of cytogenotoxicity than the reference diuron solution. This indicated that, although the intermediates C1 and C2 are not phytotoxic, they can cause cytogenotoxicity almost as severe as the intermediates C9, C10 and C11. Nevertheless, with prolonged residence time, e.g., 15 min, the cytogenotoxicity of the degradation product was dramatically reduced to a level similar to that of deionized water. It is clear that treatment with the ZnO nanorods is more effective for toxicity abatement than the conventional ZnO particles.

Cytogenotoxicity tests were also performed for the degradation products of DCA. Although DCA is benign in the sense of not inhibiting cell division, it causes aberrations at roughly the same rate as diuron. More importantly, the photocatalytic degradation of DCA does not significantly reduce this malign activity, even when the extent of degradation reaches over 80%. The degradation intermediates of DCA retain the aberration-inducing effect of the parent compound. It was also noted that, whereas the chromosomal aberrations caused by DCA itself were of metaphasic nature, the defects caused by the degradation intermediates were shifted to the interphase, prophase, and telophase. Nevertheless, the fact that such a shift was not observed in the products of diuron degradation on the ZnO nanorods, as well as the fact that the ADR was reduced to a value very close to that of pure water, suggest that the formation of DCA is not the major pathway among those in Fig. 8.

## 3. Conclusions

Diuron in aqueous solutions was successfully degraded by photocatalytic reaction on zinc oxides. The adsorption configuration of diuron on the surface of the catalysts was found to greatly affect the characteristics of the reaction, including the adsorption capacity, rate of degradation on the surface, and the degradation pathway, i.e., the structure of the intermediates formed. Electrostatic interactions between charged regions of the diuron molecule and charged surface atoms play an important role in the adsorption. The adsorption configuration was found to be surface-dependent. On (0001) and $(000\bar{1})$ polar surfaces, both the aliphatic and aromatic sides of diuron adsorb on the surface simultaneously, leading to an attack by hydroxyl radicals from both sides. However, only the aliphatic part of diuron adsorbed onto the $(10\bar{1}0)$ mixed-terminated surface is attacked because

the aromatic part is repelled from the surface. Hence, the structure of the catalyst is a crucial factor in determining the dominant degradation pathway. According to toxicity assessments, a ZnO catalyst confined by mixed-terminated surfaces, i.e., ZnO nanorods, effectively ensures the degradation of diuron by a pathway that avoids the formation of toxic intermediates.

## Acknowledgments

This research was funded by the Thailand Research Fund (No. DBG5580006). The authors also thank Naruemon Chumjai and Alisa S. Vangnai, Biocatalyst and Environmental Biotechnology Research Unit, Department of Biochemistry, Chulalongkorn University, for assistance with toxicity assessments. We thank Dr. Leo Holroyd from Edanz Group (www.edanzediting.com/ac) for editing a draft of this manuscript.

## Appendix A. Supplementary data

Supplementary data to this article can be found online at https://doi.org/10.1016/j.jes.2019.04.016.

## REFERENCES

Bouquet-Somrani, C., Fajula, F., Finiels, A., Graffin, P., Geneste, P., Olive, J.-L., 2000. Photocatalytic degradative oxidation of Diuron in organic and semi-aqueous systems over titanium dioxide catalyst. New J. Chem. 24 (12), 999–1002.

Carrier, M., Guillard, C., Besson, M., Bordes, C., Chermette, H., 2009. Photocatalytic degradation of diuron: experimental analyses and simulation of $HO^{\circ}$ radical attacks by density functional theory calculations. J. Phys. Chem. A 113 (22), 6365–6374.

Chusaksri, S., Lomda, J., Saleepochn, T., Sutthivaiyakit, P., 2011. Photocatalytic degradation of 3,4-dichlorophenylurea in aqueous gold nanoparticles-modified titanium dioxide suspension under simulated solar light. J. Hazard. Mater. 190 (1–3), 930–937.

Dabrowski, J.M., Shadung, J.M., Wepener, V., 2014. Prioritizing agricultural pesticides used in South Africa based on their environmental mobility and potential human health effects. Environ. Int. 62, 31–40.

Devipriya, S., Yesodharan, S., 2005. Photocatalytic degradation of pesticide contaminants in water. Sol. Energy Mater. Sol. Cells 86 (3), 309–348.

Evgenidou, E., Konstantinou, I., Fytianos, K., Albanis, T., 2006. Study of the removal of dichlorvos and dimethoate in a titanium dioxide mediated photocatalytic process through the examination of intermediates and the reaction mechanism. J. Hazard. Mater. 137 (2), 1056–1064.

Farre, M.J., Brosillon, S., Domenech, X., Peral, J., 2007. Evaluation of the intermediates generated during the degradation of Diuron and Linuron herbicides by the photo-Fenton reaction. J. Photochem. Photobiol. A Chem. 189 (2–3), 364–373.

Fenoll, J., Martinez-Menchon, M., Navarro, G., Vela, N., Navarro, S., 2013a. Photocatalytic degradation of substituted phenylurea herbicides in aqueous semiconductor suspensions exposed to solar energy. Chemosphere 91 (5), 571–578.

Fenoll, J., Sabater, P., Navarro, G., Perez-Lucas, G., Navarro, S., 2013b. Photocatalytic transformation of sixteen substituted phenylurea herbicides in aqueous semiconductor suspensions: intermediates and degradation pathways. J. Hazard. Mater. 244, 370–379.

Foo, K.Y., Hameed, B.H., 2010. Insights into the modeling of adsorption isotherm systems. Chem. Eng. J. 156 (1), 2–10.

Gozzo, F., 2001. Radical and non-radical chemistry of the Fenton-like systems in the presence of organic substrates. J. Mol. Catal. A Chem. 171 (1–2), 1–22.

Gyuricza, V., Fodor, F., Szigeti, Z., 2010. Phytotoxic effects of heavy metal contaminated soil reveal limitations of extract-based ecotoxicological tests. Water Air Soil Poll. 210 (1–4), 113–122.

Hall, L.W., Anderson, R.D., 2014. Temporal trends analysis of 2004 to 2012 toxicity and pesticide data for California's Central Valley water quality coalitions. J. Environ. Sci. Health, Part A 49 (3), 313–326.

Hameed, B.H., Ahmad, A.L., Latiff, K.N.A., 2007. Adsorption of basic dye (methylene blue) onto activated carbon prepared from rattan sawdust. Dyes Pigments 75 (1), 143–149.

Hasenbein, S., Lawler, S.P., Connon, R.E., 2017. An assessment of direct and indirect effects of two herbicides on aquatic communities. Environ. Toxicol. Chem. 36 (8), 2234–2244.

Kaneti, Y.V., Yue, J., Jiang, X.C., Yu, A.B., 2013. Controllable synthesis of ZnO nanoflakes with exposed $(10\bar{1}0)$ for enhanced gas sensing performance. J. Phys. Chem. C 117 (25), 13153–13162.

Katsumata, H., Sada, M., Nakaoka, Y., Kaneco, S., Suzuki, T., Ohta, K., 2009. Photocatalytic degradation of diuron in aqueous solution by platinized $TiO_2$. J. Hazard. Mater. 171 (1–3), 1081–1087.

Khongthon, W., Jovanovic, G., Yokochi, A., Sangvanich, P., Pavarajarn, V., 2016. Degradation of diuron via an electrochemical advanced oxidation process in a microscale-based reactor. Chem. Eng. J. 292, 298–307.

King, J., Alexander, F., Brodie, J., 2013. Regulation of pesticides in Australia: the Great Barrier Reef as a case study for evaluating effectiveness. Agric. Ecosyst. Environ. 180, 54–67.

Kornherr, A., French, S.A., Sokol, A.A., Catlow, C.R.A., Hansal, S., Hansal, W.E.G., et al., 2004. Interaction of adsorbed organosilanes with polar zinc oxide surfaces: a molecular dynamics study comparing two models for the metal oxide surface. Chem. Phys. Lett. 393 (1–3), 107–111.

Kornherr, A., Nauer, G.E., Sokol, A.A., French, S.A., Catlow, C.R.A., Zifferer, G., 2006. Adsorption of organosilanes at a Zn-terminated ZnO (0001) surface: molecular dynamics study. Langmuir 22 (19), 8036–8042.

Krysova, H., Krysa, J., Macounova, K., Jirkovsky, J., 1998. Photocatalytic degradation of diuron [3-(3,4-dichlorophenyl)-1,1-dimethylurea] on the layer of $TiO_2$ particles in the batch mode plate film reactor. J. Chem. Technol. Biotechnol. 72 (2), 169–175.

Lawless, D., Serpone, N., Meisei, D., 1991. Role of OH* radicals and trapped holes in photocatalysis. A pulse radiolysis study. J. Phys. Chem. 95, 5166–5170.

Li, D., Haneda, H., 2003. Morphologies of zinc oxide particles and their effects on photocatalysis. Chemosphere 51 (2), 129–137.

Li, J., Wang, J., Zhang, G.K., Li, Y., Wang, K., 2018. Enhanced molecular molecular oxygen activation of $Ni^{2+}$-doped $BiO_{2-x}$ nanosheets under UV, visible and near-infrared irradiation: mechanism and DFT study. Appl. Catal. B-Environ. 234, 167–177.

Li, J., Wu, X.Y., Wan, Z., Chen, H., Zhang, G.K., 2019. Full spectrum light driven photocatalytic in-situ epitaxy of one-unit-cell $Bi_2O_2CO_3$ layers on $Bi_2O_4$ nanocrystals for highly efficient photocatalysis and mechanism unveiling. Appl. Catal. B-Environ. 243, 667–677.

Liu, B., Zeng, H.C., 2003. Hydrothermal synthesis of ZnO nanorods in the diameter regime of 50 nm. J. Am. Chem. Soc. 125 (15), 4430–4431.

Malato, S., Blanco, J., Caceres, J., Fernandez-Alba, A.R., Aguera, A., Rodriguez, A., 2002. Photocatalytic treatment of water-soluble

pesticides by photo-Fenton and $TiO_2$ using solar energy. Catal. Today 76 (2–4), 209–220.
Malato, S., Caceres, J., Fernandez-Alba, A.R., Piedra, L., Hernando, M.D., Aguera, A., et al., 2003. Photocatalytic treatment of diuron by solar photocatalysis: evaluation of main intermediates and toxicity. Environ. Sci. Technol. 37 (11), 2516–2524.
Meephon, S., Rungrotmongkol, T., Kaiyawet, N., Puttamat, S., Pavarajarn, V., 2018. Surface-dependence of adsorption and its influence on heterogeneous photocatalytic reaction: a case of photocatalytic degradation of linuron on zinc oxide. Catal. Lett. 148, 873–881.
Montoya, J.F., Atitar, M.F., Bahnemann, D.W., Peral, J., Salvador, P., 2014. Comprehensive kinetic and mechanistic analysis of $TiO_2$ photocatalytic reactions according to the direct-indirect model: (II) experimental validation. J. Phys. Chem. C 118 (26), 14276–14290.
Pacchioni, G., 1993. Physisorbed and chemisorbed $CO_2$ at surface and step sites of the MgO(100) surface. Surf. Sci. 281 (1–2), 207–219.
Parra, M.R., Haque, F.Z., 2014. Aqueous chemical route synthesis and the effect of calcination temperature on the structural and optical properties of ZnO nanoparticles. J. Mater. Res. Technol. 3 (4), 363–369.
Prieto-Rodriguez, L., Miralles-Cuevas, S., Oller, I., Aguera, A., Puma, G.L., Malato, S., 2012. Treatment of emerging contaminants in wastewater treatment plants (WWTP) effluents by solar photocatalysis using low $TiO_2$ concentrations. J. Hazard. Mater. 211, 131–137.
Silambarasan, S., Vangnai, A.S., 2016. Biodegradation of 4-nitroaniline by plant-growth promoting *Acinetobacter* sp. AVLB2 and toxicological analysis of its biodegradation metabolites. J. Hazard. Mater. 302, 426–436.
Sivakumar, P., Palanisamy, P., 2009. Adsorption studies of Basic Red 29 by a non-conventional activated carbon prepared from *Euphorbia antiquorum* L. Int. J. Chem. Tech. Res. 1 (3), 502–510.
Souza, P.M.S., Corroque, N.A., Morales, A.R., Marin-Morales, M.A., Mei, L.H.I., 2013. PLA and organoclays nanocomposites: degradation process and evaluation of ecotoxicity using *Allium cepa* as test organism. J. Polym. Environ. 21 (4), 1052–1063.
Steiner, T., 1997. Unrolling the hydrogen bond properties of C-H···O interactions. Chem. Commun. 727–734.
Steiner, T., 2002. The hydrogen bond in the solid state. Angew. Chem. Int. Edit. 41 (1), 48–76.
Sun, K., Zhang, Z., Gao, B., Wang, Z., Xu, D., Jin, J., et al., 2012. Adsorption of diuron, fluridone and norflurazon on single-walled and multi-walled carbon nanotubes. Sci. Total Environ. 439, 1–7.
Tian, J.T., Wang, J.F., Dai, J.H., Wang, X., Yin, Y.S., 2009. N-doped $TiO_2$/ZnO composite powder and its photocatalytic performance for degradation of methyl orange. Surf. Coat. Tech. 204 (5), 723–730.
Tixier, C., Bogaerts, P., Sancelme, M., Bonnemoy, F., Twagilimana, L., Cuer, A., et al., 2000. Fungal biodegradation of a phenylurea herbicide, diuron: structure and toxicity of metabolites. Pest Manag. Sci. 56 (5), 455–462.
Turchi, C.S., Ollis, D.F., 1990. Photocatalytic degradation of organic water contaminants: mechanisms involving hydroxyl radical attack. J. Catal. 122 (1), 178–192.
Wang, J.L., Xu, L.J., 2012. Advanced oxidation processes for wastewater treatment: formation of hydroxyl radical and application. Crit. Rev. Environ. Sci. Technol. 42 (3), 251–325.
Wang, C., Xu, B.-Q., Wang, X., Zhao, J., 2005. Preparation and photocatalytic activity of ZnO/$TiO_2$/$SnO_2$ mixture. J. Solid State Chem. 178 (11), 3500–3506.
Wang, K., Wu, X.Y., Zhang, G.K., Li, J., Li, Y., 2018. $Ba_5Ta_4O_{15}$ nanosheet/$AgVO_3$ nanoribbon heterojunctions with enhanced photocatalytic oxidation performance: hole dominated charge transfer path and plasmonic effect insight. ACS Sustain. Chem. Eng. 6 (5), 6682–6692.
Woll, C., 2007. The chemistry and physics of zinc oxide surfaces. Prog. Surf. Sci. 82 (2–3), 55–120.
Woo, O.T., Chung, W.K., Wong, K.H., Chow, A.T., Wong, P.K., 2009. Photocatalytic oxidation of polycyclic aromatic hydrocarbons: intermediates identification and toxicity testing. J. Hazard. Mater. 168 (2–3), 1192–1199.
Yu, W.L., Xu, D.F., Peng, T.Y., 2015. Enhanced photocatalytic activity of g-$C_3N_4$ for selective $CO_2$ reduction to $CH_3OH$ via facile coupling of ZnO: a direct Z-scheme mechanism. J. Mater. Chem. A 3 (39), 19936–19947.
Yuan, R.X., Ramjaun, S.N., Wang, Z.H., Liu, J.S., 2012. Photocatalytic degradation and chlorination of azo dye in saline wastewater: kinetics and AOX formation. Chem. Eng. J. 192, 171–178.